JOURNAL OF GEOPHYSICAL RESEARCH, VOL. 113, C03002, doi:10.1029/2007JC004143, 2008

Scaling properties of sea ice deformation from buoy dispersion analysis

P. Rampal,[1,2] J. Weiss,[1] D. Marsan,[2] R. Lindsay,[3] and H. Stern[3]

Received 5 February 2007; revised 3 September 2007; accepted 15 November 2007; published 4 March 2008.

[1] A temporal and spatial scaling analysis of Arctic sea ice deformation is performed over timescales from 3 h to 3 months and over spatial scales from 300 m to 300 km. The deformation is derived from the dispersion of pairs of drifting buoys, using the IABP (International Arctic Buoy Program) buoy data sets. This study characterizes the deformation of a very large solid plate (the Arctic sea ice cover) stressed by heterogeneous forcing terms like winds and ocean currents. It shows that the sea ice deformation rate depends on the scales of observation following specific space and time scaling laws. These scaling properties share similarities with those observed for turbulent fluids, especially for the ocean and the atmosphere. However, in our case, the time scaling exponent depends on the spatial scale, and the spatial exponent on the temporal scale, which implies a time/space coupling. An analysis of the exponent values shows that Arctic sea ice deformation is very heterogeneous and intermittent whatever the scales, i.e., it cannot be considered as viscous-like, even at very large time and/or spatial scales. Instead, it suggests a deformation accommodated by a multiscale fracturing/faulting processes.

Citation: Rampal, P., J. Weiss, D. Marsan, R. Lindsay, and H. Stern (2008), Scaling properties of sea ice deformation from buoy dispersion analysis, *J. Geophys. Res.*, *113*, C03002, doi:10.1029/2007JC004143.

1. Introduction

[2] The Arctic sea ice cover is a deforming solid which extends during winter over about 14 million km, with an average thickness of a few meters. Consequently, it can be considered, from a mechanical point of view, as a two dimensional plate (plane stress conditions are fulfilled). This plate deforms under various stresses, mainly from winds and ocean currents [*Thorndike and Colony*, 1982]. This leads to the fracturing and faulting of the sea ice cover. The overall sea ice deformation, along with thermodynamics, controls the amount of open water as well as the ice thickness distribution: divergent deformation is associated with crack opening and new ice growth, whereas convergent deformation causes ice to pile up and ridges to form. Sea ice deformation is important for understanding the momentum, mass, and energy balance in the Arctic and more generally the influence of Arctic dynamics on the Earth's climate. Fracturing and divergence of the ice cover decreases the albedo and allows more shortwave absorption by the ocean, thereby shrinking the ice cover during summer, and possibly reducing its strength and increasing the fracturing [*Zhang*, 2001; *Moritz et al.*, 2002] and the faulting [*Kwok*, 2001, 2006]. On the other hand, fracturing during winter enhances the thermodynamically driven production of new ice and consequently modifies the heat and salinity budget in the Arctic Ocean [*Maykut*, 1982]. These complex processes are highly non-linear. As an example, in an ice cover fractured with 0.5% of open water leads, 50% of the thermal energy lost from the ocean occurs along these leads [*Heil and Hibler*, 2002]. In what follows, we used the term "fracturing" in a generic sense. I.e., it refers to tensile fracturing (opening mode) as well as to shear faulting indifferently.

[3] Sea ice dynamics models implemented in climate models are based on a continuum mechanics modeling framework initially developed by *Hibler* [1979], and share a common viscous-plastic (VP) or elastic-viscous-plastic (EVP; *Hunke and Dukowicz*, 1997) rheology. This rheology implies that for stress states inside the plastic yield curve, sea ice behaves as a viscous fluid (with an additional linear elastic component for EVP rheology), while ice flows as a perfect plastic when the stress state reaches the envelope, without further increase of the stress. This viscous flow is considered to result from the average effect of many "plastic" events [*Hibler*, 1977], and as such relies on an hypothesis that the stress and strain are locally homogeneous or smoothly varying. This framework has been widely used, as it is suited for a numerical coupling with other fluid layers (ocean, atmosphere), and because of the development of efficient methods to solve the momentum equation employing this rheology [*Zhang*, 2001]. By construction, it homogenizes the sea ice properties at the discretization scale, and therefore ignores possible sub-grid scale variability.

[1]Laboratoire de Glaciologie et Géophysique de l'Environnement, CNRS, Université Joseph Fourier-Grenoble, France.
[2]Laboratoire de Géophysique Interne et Tectonophysique, CNRS, Université de Savoie-Le Bourget du Lac, France.
[3]Polar Science Center, Applied Physics Laboratory, University of Washington, Seattle, Washington, USA.

0148-0227/08/2007JC004143$09.00

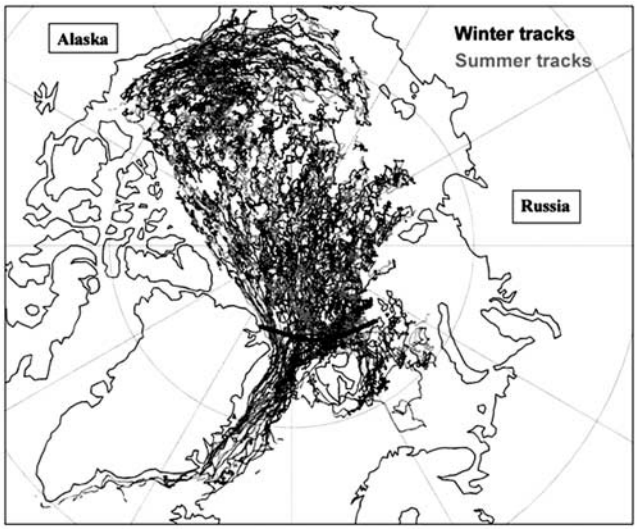

Figure 1. Map of the Arctic basin showing approximately 500 buoy tracks from the IABP (International Arctic Buoy Program) data set, recorded between 1979 and 2002. The bold arc represents the lower geographical limit of the data used in our analysis.

[4] Recent analyses of deformation and fracturing fields over the Arctic sea ice cover challenged this classical modeling framework in two ways: the viscous-plastic rheology assumption and the homogeneous stress and strain assumption. A detailed analysis of in situ ice stresses and satellite-derived strain rates showed that stress states are indeed confined in an envelope with Coulombic branches, but its size is rate- and scale-dependent [*Weiss et al.*, 2007]. Moreover, no correlation was observed between stress and strain rate, in contradiction to a viscous behavior. A multifractal analysis of strain rate fields obtained from RGPS (Radarsat Geophysical Processor System [*Kwok*, 1998]) demonstrated the highly heterogeneous, scale-free character of sea ice deformation [*Marsan et al.*, 2004], therefore raising doubts about the homogeneous assumption used in sea ice models. Similarly, in situ ice stress records are highly intermittent and scale-invariant in time [*Weiss and Marsan*, 2004]. All these observations argue for an elasto-brittle behavior of the sea ice cover, as suggested by *Nye* [1973], with a deformation accommodated by multiple fractures and faults at various scales. However, these recent analyses had limitations: RGPS has a limited time resolution of about 3 days, and in situ ice stress data are local and not necessarily representative of the large areas. A comprehensive scaling analysis of sea ice deformation, covering a wide range of both time and spatial scales is therefore needed.

[5] In this paper, we describe the fracturing and faulting of the ice in terms of deformation. We show the time and spatial scale invariance properties of sea ice deformation, improving the time and spatial ranges of analysis compared to previous studies. The resulting scaling laws and associated exponents are guidelines for understanding the underlying physics of the mechanisms of sea ice deformation and dynamics.

[6] The consequence of sea ice fracturing and faulting is that, like two particles in a gas or two people in a crowd, two nearby pieces of sea ice gradually move apart and disperse [*Martin and Thorndike*, 1985]. Thus to study the dispersion of sea ice is a way to analyze its deformation. Considering two pieces of sea ice, each of them holding a buoy capable of reporting its position through time, we can analyze the dispersion of sea ice in terms of the changes in separation between this pair of buoys. This idea was first proposed and applied to Arctic sea ice by *Martin and Thorndike* [1985]. Their study revealed, in a statistical sense, similarities between the dispersion properties of sea ice and the dispersion of particles in turbulent fluids, even if we expect that the underlying physics is not the same. The dispersion process is a phenomenon which has been defined and studied for a long time for turbulent fluids. Rather than following buoys fixed to the sea ice, these studies of fluids followed colored tracers in gases or liquids, balloons in the atmosphere, or buoys at the surface of the ocean [*Richardson and Stommel*, 1949; *Batchelor*, 1951; *Okubo*, 1971; *Morel and Larchevèque*, 1974; *Martins et al.*, 2002; *Zhang et al.*, 2000; *Jullien et al.*, 1999]. In this paper, we follow the idea initially proposed by *Martin and Thorndike* [1985], with a much larger data set, representative of the entire Arctic Ocean. To study sea ice deformation, we follow a methodology inspired from the analysis of fluid turbulence, and particularly the analysis of oceanic and atmospheric turbulence, which provide two main forcing terms of sea ice dynamics. Similarities and differences between sea ice dynamics and fluid turbulence are stressed to understand the coupling between the different layers of the system and the nature of sea ice deformation.

2. Data Set: Trajectories of Drifting Buoys

[7] The data set, provided by the International Arctic Buoy Program (http://iabp.apl.washington.edu/), consists of trajectories of drifting buoys which were deployed in the Arctic between 1979 and 2002. A total of approximately 500 drifting buoys were installed over the entire Arctic basin during this period. The buoys are fixed on the ice and drift according to the ice motion. Buoy trajectories plotted in Figure 1 clearly show that our data set is representative of the whole Arctic Ocean. However, the lifetime of each buoy is variable, from a few days to many months. We only kept the positions contained in the Arctic basin, above the bold arc drawn on Figure 1.

[8] We worked more specifically on pairs of simultaneously active buoys, approximately 680 pairs, or 500,000 three-hourly geographical positions obtained between 1979 and 2002: 70% were recorded in winter (i.e., from mid-September to mid-June) and the remainder in summer. The average sampling rate of the raw data was 1 position per hour. The raw data were post-processed by the IABP by determining a cubic interpolation of the geographical positions and then re-sampling the interpolated trajectories at 3-h intervals. Buoys that rely on the ARGOS system for position estimates have a position uncertainty of about 100 to 300 m (depending on the measurement quality), while those that use GPS have an uncertainty of about 100 m.

[9] In their analysis of buoy dispersion, *Martin and Thorndike* [1985] used a similar, although much smaller, data set. It consisted of two sets, each of about a dozen drifting buoys, which were launched in the Bering and

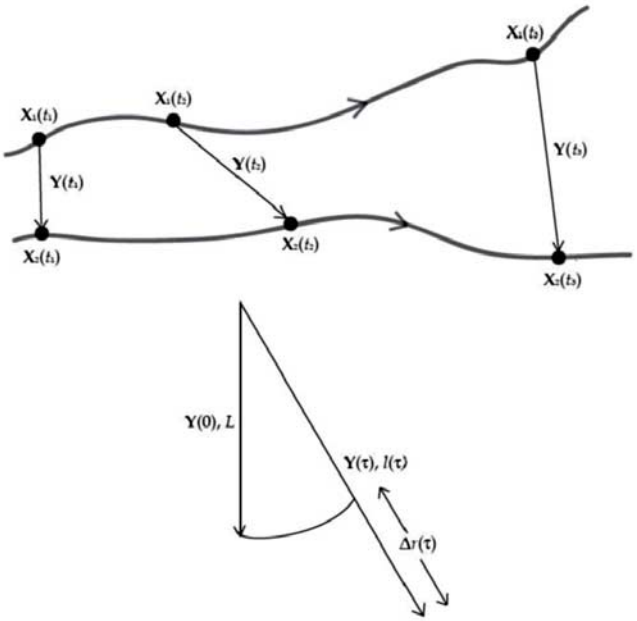

Figure 2. For a pair of buoys located at $\overrightarrow{X_1}$, $\overrightarrow{X_2}$, the separation $\overrightarrow{Y} = \overrightarrow{X_2} - \overrightarrow{X_1}$ yields the dispersion $\Delta r = \|\overrightarrow{Y}(\tau) - \overrightarrow{Y}(0)\|$ at time τ.

Beaufort Seas in the winter, and which recorded their positions during several days with a sampling rate of 1 position per hour. They analyzed the dispersion within the scale ranges of 1 h to 4 days, and from a few km to 60 km.

[10] As another point of comparison, *Marsan et al.* [2004] used the RGPS data which is derived from synthetic aperture radar (SAR) images. These images are used to track the trajectories of about 40,000 points over the entire Arctic for periods of up to 6 months. The points are initially spaced 10 km apart and are organized into four-cornered cells. From these trajectories, the strain rates can be calculated over each cell, at an average sampling interval of 3 days. This allows analysis of the scaling of sea ice deformation from 10 km to 1000 km, at the timescale of 3 days. This timescale represents a limitation of the RGPS data set for scaling analyses [*Marsan et al.*, 2004].

[11] Compared to these former analyses, our data set presents (i) a much greater spatial coverage and statistical representation, as well as larger temporal and spatial ranges than the *Martin and Thorndike* [1985] data set and, (ii) a much better time resolution than the RGPS data set, allowing small timescales to be explored.

3. Methodology

[12] The methodology used in this work to analyze the deformation of a solid plate from the dispersion of passive tracers is inspired by a classical methodology developed in fluid turbulence [*Richardson and Stommel*, 1949; *Batchelor*, 1951]. We study how the dispersion of pairs of buoys depends on both (1) their initial separation L, and (2) the time τ during which they disperse. In Figure 2, two buoys A and B with absolute positions $\vec{X}_1$ and $\vec{X}_2$ respectively, and with separation $\vec{Y} = \vec{X}_2 - \vec{X}_1$, are considered. If these two buoys initially separated by $L = \|\vec{Y}(0)\|$ are observed after a time $t = \tau$, a change in separation is observed. Our notations are: $\vec{Y}(0)$ has magnitude L and $\vec{Y}(\tau)$ has magnitude $l(\tau)$. We define the change in separation Δr as:

$$\Delta r = \|\vec{Y}(\tau)\| - \|\vec{Y}(0)\| = l(\tau) - L \tag{1}$$

In fluid mechanics, the dispersion process is characterized by the mean square change in separation $\langle \Delta r^2 \rangle$. Except for section 3, this variable is not considered here. From a solid mechanics perspective, it appears more pertinent to consider the rate $\dot{D} = \Delta r / L\tau$ instead of the change in separation Δr. $\dot{D}$ is analogous to a deformation rate, measured in day^{-1}. Neither Δr nor $\dot{D}$ are sensitive to solid rotations. They only quantify the deformation due to divergence, convergence, and/or shear.

[13] When analyzing the whole Arctic basin (see section 4), we made a distinction between winter (from mid-September to mid-June) and summer. Separately for both seasons, we computed the distributions of $\dot{D}$ for various L and τ ranging from a few kilometers to 500 km and from 3 h to several months (one month for summer). For each space-time interval, the associated distribution is characterized by its standard deviation $\sigma_{\dot{D}}$, which is a function of L and τ. In this way, we measure how a cluster of passive tracers of initial size L typically disperses after a time τ or, in other words, how the associated region containing these tracers deforms (We will show in the next section two examples of how deformation and dispersion can be linked). The choice of the standard deviation of $\dot{D}$ rather than its mean is partly motivated by the fact that in the limit of small deformation rate (i.e., for large time and spatial scales), only the standard deviation allows to characterize the deformation process. We checked this by calculating the two parameters for each computed distribution of $\dot{D}$ (i.e., corresponding to each $L - \tau$ interval). We observed that the standard deviation of $\dot{D}$ evolved over the entire L and τ ranges, whereas the mean remained insensitive to sea ice deformation at large spatial scales. In addition, the choice of the standard deviation was motivated by an analogy with the methodology used in fluid turbulence to characterize the dispersion of passive tracers.

[14] The number N of measurements available in each $L - \tau$ interval for the distribution of $\dot{D}$ is extremely variable, ranging from 920 to 812,405 in winter, and from 6 to 257,871 in summer. From these N measurements, many values can come from a single pair of buoys and thus are not independent. Indeed, the autocorrelation analysis of $\dot{D}$ time records for an initial separation of $L \sim 300$ km shows a correlation time of approximately 10 h. Thus we only kept one $\dot{D}$-value in three provided by each pair of buoys. Moreover, the distributions of $\dot{D}$ are clearly not Gaussian, with significantly slower decays toward large values (this aspect will be detailed in future work). All these observations suggest that we would under-estimate the errors $\Delta\sigma_{\dot{D}}$ on $\sigma_{\dot{D}}$ if we were to estimate it as $\Delta\sigma_{\dot{D}}/\sigma_{\dot{D}} \sim N^{-0.5}$, i.e., using the central limit theorem. Instead, we estimated $\Delta\sigma_{\dot{D}}$ from a bootstrap method described in Appendix 1, which led us to

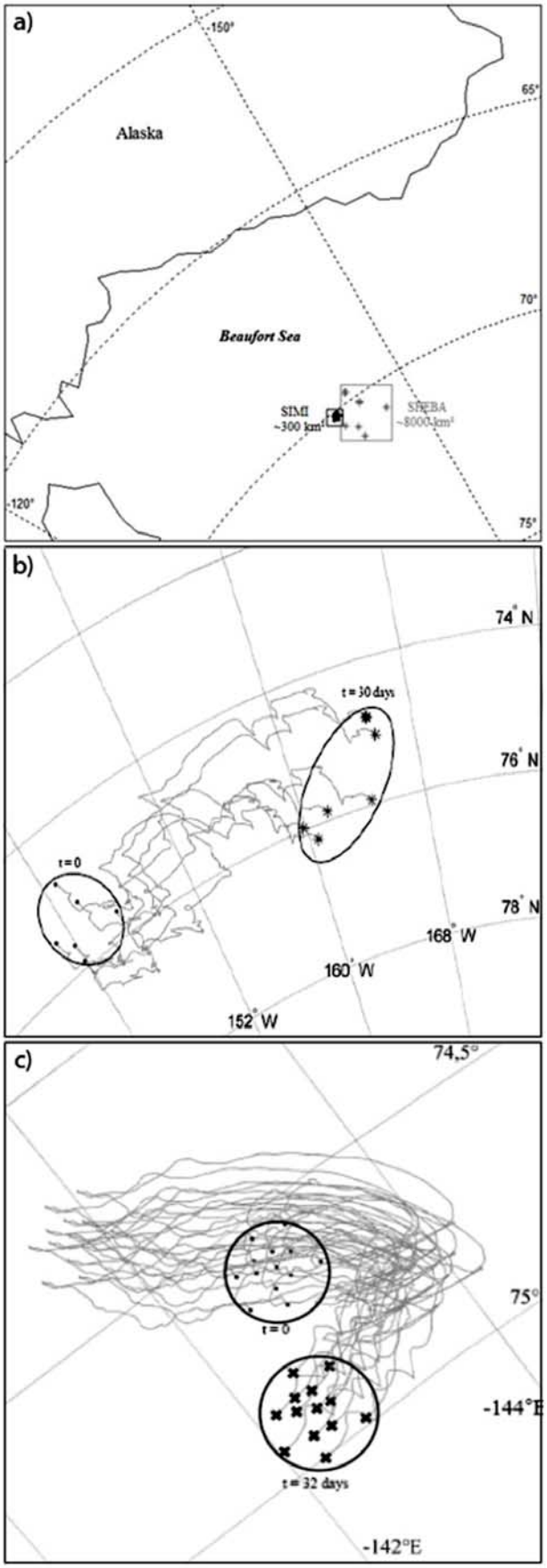

consider, instead of the number of samples, the number of pairs of buoys as an independent variable.

4. Introduction to the Dispersion Process: Two Examples of Buoy Dispersions

[15] Most buoys are typically not clustered sufficiently well to determine the deformation as a cluster, although they can be easily grouped into pairs to estimate the dispersion (detailed in section 2). However, two field projects ("SHEBA", Surface Heat Budget of the Arctic Ocean, and "SIMI", Sea Ice Mechanics Initiative) provide an opportunity to determine the relationship between two-point dispersion estimates of the deformation and multipoint (cluster) deformation estimates found by fitting a linear function of the velocity to the buoy positions. The buoys were deployed by the Cold Regions Research and Engineering Laboratory (the data sets are available on the Web: www.crrel.usace.army.mil/sid/SeaIceDynamics/).

[16] The experiments took place in the western Arctic close to the Alaskan coast (Figure 3a) in winters 1997–1998 for SHEBA and 1993–1994 for SIMI. For each experiment, a set of N_b buoys is considered ($N_b = 6$ and 13 respectively), and we use the positions of the buoys over a period of approximately one month. At the beginning of this period the buoys form clusters of different initial sizes, $L^2 \sim 300$ km^2 for SIMI and 8000 km^2 for SHEBA. Through time, these clusters deform. The two sets of trajectories are drawn on Figure 3b and Figure 3c with the positions of the clusters at the beginning and at the end of the period indicated. We illustrate here the link between the deformation of the underlying solid plate and the dispersion of buoys:

[17] We follow a cluster of buoys between times t and $t + \Delta t$ (Δt = 1h) and estimate at various times t the strain tensor $\varepsilon_{ij}(t)$ from each set of buoys. The actual deformation of the two sets of buoys shows spatial variability: it is not homogeneous over the whole region encompassed by the buoys. However, here we follow the deformation at the scale of those regions (~300 km^2 and ~8000 km^2), and therefore assume a smooth, i.e., homogeneous, process for these observables. So we calculate the best coefficients of the matrix M_{ij} which minimizes $\sum_k (\vec{U}_k - M_{ij}\vec{X}_k)^2$, where $\vec{U}_k$ is the displacement vector of the kth buoy during Δt and $\vec{X}_k$ its position at time t. M_{ij} is the matrix of the displacement gradients. We compute the strain tensor ε_{ij} from M_{ij} as:

$$\varepsilon_{ij} = \frac{1}{2}\left(M_{ij} + M_{ji}\right) \tag{2}$$

Figure 3. (a). Map showing the "SHEBA" and "SIMI" regions, and the initial positions of the buoys. An estimate of the surface area delimited by the two sets of buoys is ~300 km^2 for SIMI and ~8000 km^2 for SHEBA. (b). Tracks of the six SHEBA buoys. These correspond to a 30-day drift from the 27th of October to the 24th of November, 1997. The smallest ellipse including all the buoys at t = 0 and t = 30 days is drawn in black. Its form evolves through time, illustrating the sea ice deformation of the respective region, with combination of shear and divergence components. (c). Same as (b) for the 13 SIMI buoys. Compared to SHEBA, the deformation is weaker.

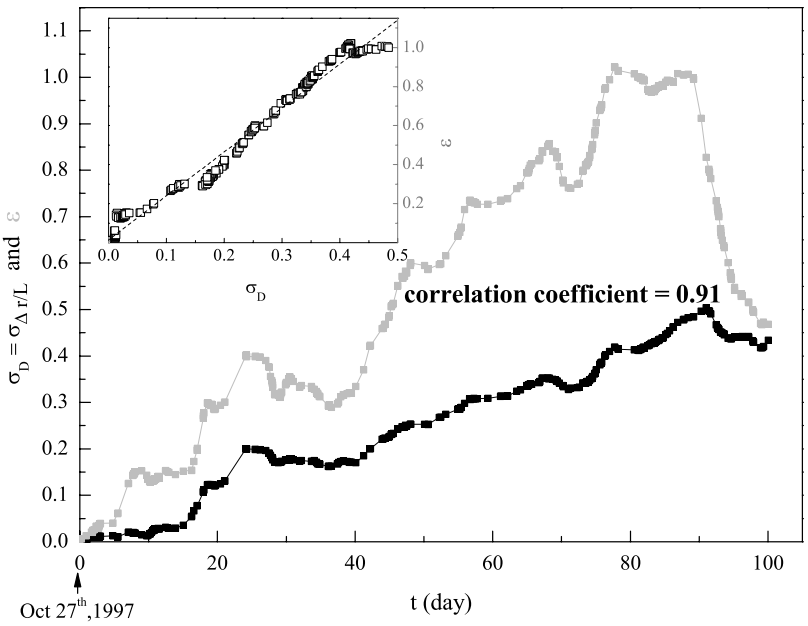

Figure 4. Standard deviation σ_D of the deformation D (computed from the dispersion of pairs of buoys), and of the strain ε_{tot} versus time t, for the SHEBA experiment. The inset plot shows the proportionality between the both (the slope of the dashed line is about 2.25 +/− 0.01).

[18] Then we compute two invariants of the deformation, the divergence and the shear strain:

$$div = tr(\varepsilon_{ij}) \tag{3}$$

$$shr = \left[(\varepsilon_{11} - \varepsilon_{22})^2 + (\varepsilon_{12} + \varepsilon_{21})^2\right]^{1/2} \tag{4}$$

[19] Finally, we deduce the magnitude of the total deformation as:

$$\varepsilon_{tot} = \sqrt{div^2 + shr^2} \tag{5}$$

[20] Figure 4 shows this deformation ε_{tot} along with the standard deviation σ_D of the deformation $D = \Delta r/L$ derived from the dispersion of the SHEBA buoys over a period of 100 days. We obtain a correlation coefficient of 0.91 between them, although σ_D is systematically smaller than ε_{tot}. It can be shown by simple Monte-Carlo simulations assuming homogeneous deformation that ε_{tot} is typically greater than σ_D by a factor of 4 on average with a standard deviation of about approximately 3. These simulations do not take into account the existing spatial correlations of the buoys trajectories. Therefore this factor of proportionality is an upper bound estimate. For example, in a realistic case like SHEBA, the buoys trajectories are spatially correlated, i.e., disperse less than one would expect for an equivalent cluster with uncorrelated trajectories, and this factor is less (i.e., approximately 2) (see the inset graph in Figure 4). We note also the large standard deviation associated with this ratio (i.e., 3). Consequently, the value of 2.25 obtained for SHEBA is not necessarily representative of the general case. In the case of SIMI, we look at the deformation of a "small" initial region (about 300 km^2) compared to the SHEBA's one (about 8000 km^2). Then, the dispersion is expected to be smaller too in magnitude (see details in the next paragraph), i.e., the relative displacements leading to this dispersion are smaller. This implies that the "signal over noise" (e.g., due to the position uncertainty) ratio is larger for SIMI than for SHEBA. Consequently, we found a less good correlation between ε_{tot} and σ_D for SIMI (e.g., ~0.65). In conclusion, this evidence shows that the sea ice deformation can be approximated by following the dispersion of pairs of passive tracers.

[21] We also compute the mean square change in separation $\langle \Delta r^2 \rangle = \langle (r(t+\tau) - r(t))^2 \rangle$ as a function of τ (Figure 5). The number of values of Δr for each distribution ranged from 465 to 109,122. $\langle \Delta r^2 \rangle$ is a quantity which characterizes the dispersion process [*Richardson*, 1926]. The magnitude of the dispersion is larger for SHEBA than for SIMI. However, *Martin and Thorndike* [1985] obtained, for an initial cluster of intermediate size (~2500 km^2), greater magnitudes than those for SHEBA and SIMI. We can reasonably imagine that stronger wind-forcing and a thinner ice cover in the Bering Sea region (marginal sea of the Arctic basin) can lead to such large magnitudes of dispersion. The evolution of $\langle \Delta r^2 \rangle$ can be approximated by a power law scaling $\langle \Delta r^2 \rangle \sim \tau^{\gamma}$, with γ ranging between 1 and 3. We find that $\gamma \simeq 1.6$ for SHEBA whereas, for SIMI, $\gamma \simeq 1.6$ for $\tau < 1$ day, and $\gamma \simeq 0.6$ for $\tau > 1$ day. We note here that molecular dispersion is characterized by $\langle \Delta r^2 \rangle \sim \tau$ [*Einstein*, 1905], whereas atmospheric turbulence is characterized by $\langle \Delta r^2 \rangle \sim \tau^3$ [*Richardson*, 1926]. In other words, sea ice deformation in these two regions is found to be characterized by a super-diffusive regime, although there is a hint for a sub-diffusive regime in the SIMI experiment for timescales greater than 1 day.

[22] The significant variation of γ from one experiment to another stresses the need to consider ensemble averages over the whole Arctic basin rather than particular regional

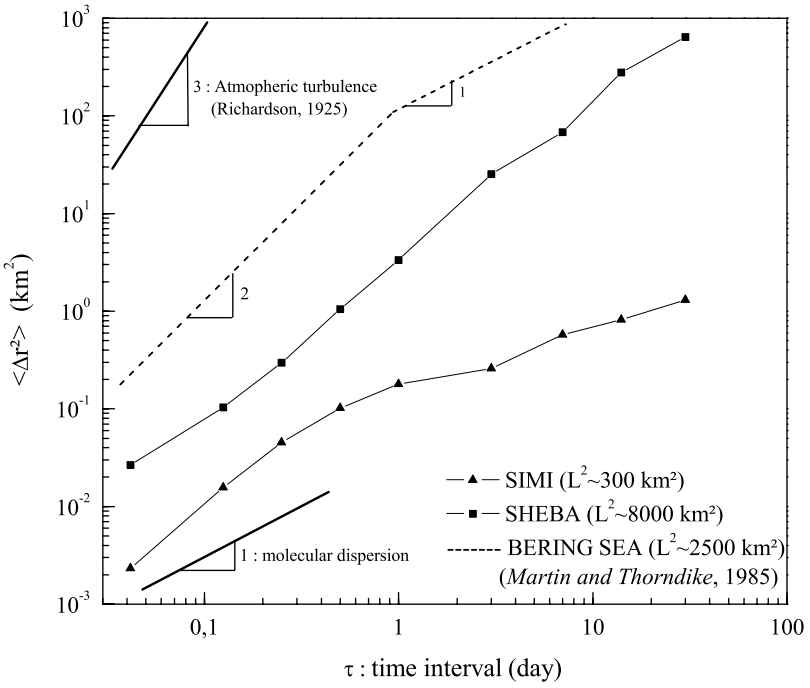

Figure 5. $\langle \Delta r^2 \rangle$ versus the time interval τ for the SHEBA and SIMI clusters. The dashed line shows the results of *Martin and Thorndike* [1985] for their initial cluster of 2500 km^2. The lines with slope 1 and 3 are for reference only.

experiments in order to obtain a global characterization of sea ice deformation. A comparison with the results of *Martin and Thorndike* [1985] illustrates this idea: they showed that for an area of about 2500 km^2 located in the Bering Sea $\langle \Delta r^2 \rangle \sim \tau^2$ for $\tau < 1$ day, and $\langle \Delta r^2 \rangle \sim \tau$ for $\tau > 1$ day. The SIMI experiment is in relative agreement with this former study, whereas we obtained a different power law without any change in regime within the 3 h-30 days interval for SHEBA.

[23] A $\langle \Delta r^2 \rangle \sim \tau$ regime implies separation velocities increasing as $\Delta r/\tau \sim \Delta r^{-1}$ with decreasing Δr. Physically, this velocity cannot increase indefinitely toward small scales. So a change in regime, so that the velocity becomes constant (ballistic regime, with $\langle \Delta r^2 \rangle$ evolving as τ^2), is expected to occur at short timescales [*Taylor*, 1921]. We did not observe this regime change with SHEBA, because the transition must occur at a characteristic time that is less than our resolution (i.e., for $\tau < 1$ h).

[24] Finally, we calculate the standard deviation $\sigma_{\dot{D}}$ of the deformation rate $\dot{D} = \Delta r/L\tau$, as well as the strain rate $\dot{\varepsilon}_{tot}$ (Figure 6). Here, we consider the characteristic scale L instead of L^2. The magnitude of $\sigma_{\dot{D}}$ is larger for the small cluster (i.e., SIMI) than for the large one (i.e., SHEBA), at short times τ, implying a stronger deformation rate at small spatial scales. In addition, $\sigma_{\dot{D}}$ reasonably fits a power law $\sigma_{\dot{D}} \sim \tau^{-\alpha(L)}$. The exponent α is different for the two experiments, with $\alpha = 0.7$ for small spatial scale (SIMI), and $\alpha = 0.2$ for the large spatial scale (SHEBA). These exponents are consistent with the exponents found for $\langle \Delta r^2 \rangle$ in the following way:

$$\sigma_{\dot{D}} \sim \tau^{-\alpha} \sim \dot{D} \sim \Delta r/L\tau \sim \tau^{\gamma/2-1} \qquad (6)$$

[25] Hence $\alpha = 1 - \gamma/2$. For the SHEBA experiment, we can effectively check that: $\alpha = 1 - (1.6/2) = 0.2$. The systematic dependence of α with respect to L (or L^2) is discussed in section 5. We also note that the two calculations of deformation rates, the first one from the strain rate tensor and the second one from the dispersion rate, lead to very similar power law trends. This confirms that one may use the dispersion of buoys to accurately estimate sea ice deformation rates, and the associated scaling laws.

[26] To summarize, this analysis of two clusters of buoys shows that:

[27] (i) Arctic sea ice disperses as the result of deformation. Our two examples and the one of *Martin and Thorndike* [1985], which correspond to different periods and regions of the Arctic, show similar qualitative trends but significantly different scaling exponents. This illustrates the strongly heterogeneous character of sea ice deformation, thus the need for ensemble averages to estimate robust scaling. Moreover, deformation rates decrease with the increasing time interval τ considered, highlighting the intermittency of this process.

[28] (ii) The intensity of the dispersion and the magnitude of the deformation rates depend on both spatial and temporal scales.

[29] (iii) Both dispersion and deformation rates scale with the time interval τ as power laws.

[30] (iv) These exponents depend on the spatial scale L (or L^2). As L increases, the dispersion increases whereas the deformation decreases. This implies a non-trivial coupling between space and time in the dispersion/deformation process.

[31] These two experiments only concern limited spatial and timescales, and specific regions of the Arctic basin.

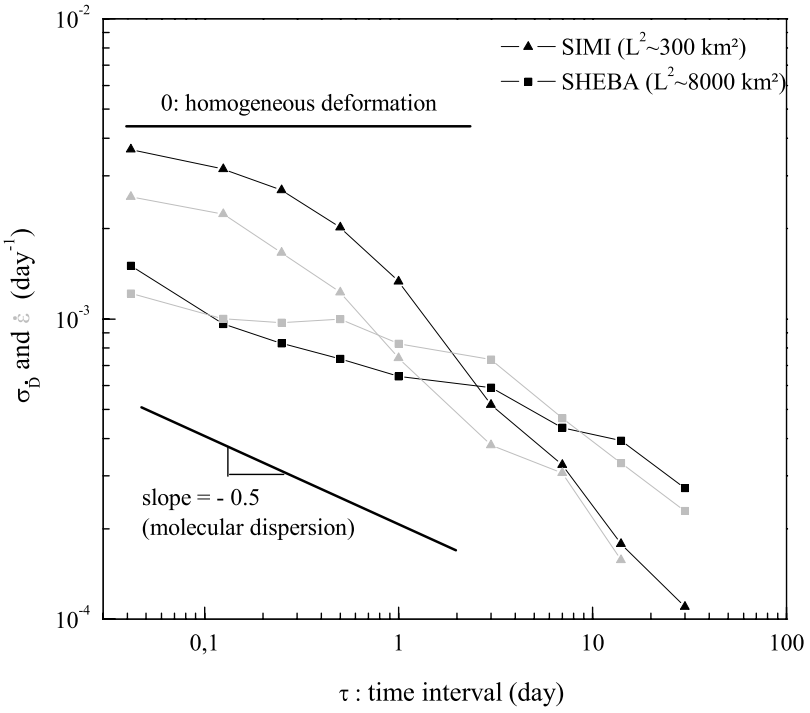

Figure 6. Strain rate $\dot{\varepsilon}_{tot}$ and its proxy $\sigma_{\dot{D}}$ (standard deviation of $\dot{D}$) versus τ for the SHEBA and SIMI experiments. The horizontal line and the line with slope -0.5 are for reference only.

Thanks to the exceptional data set provided by IABP, we can extend the analysis to the whole Arctic Ocean and up to a timescale of several months.

5. Sea Ice Dispersion and Deformation Over the Whole Arctic Ocean: Results

[32] We now consider the time and spatial scaling of sea ice deformation rate for the whole Arctic Ocean, based on the dispersion of pairs of buoy trajectories (Figure 1).

5.1. Time Scaling

[33] Figure 7a and Figure 7b show the standard deviation of the deformation rate $\sigma_{\dot{D}}$ versus the time interval of observation τ for winter and summer, respectively. Because of the small number of independent observations for some distributions, the errors on $\sigma_{\dot{D}}$ can be very large, as mentioned in section 2. The estimation of these errors bars is detailed in Appendix 1; they increase as the timescale increases and the spatial scale decreases. We observe a power law scaling, $\sigma_{\dot{D}} \sim \tau^{-\alpha(L)}$, over 3 orders of magnitude.

[34] The exponents α were determined using a weighted least squares algorithm (The weights depending on the error bars). The corresponding errors in the calculation of the slopes range from 7% to 25%. The exponents α increase with decreasing initial separation L, ranging from 0.89 for $L = 1$ km to 0.30 for $L = 300$ km in winter and from 0.87 for $L = 1$ km to 0.25 for $L = 300$ km in summer (Figure 8). Thus we note that the seasons cannot be distinguished in terms of scaling exponents.

[35] The apparent change of slope value between the power law for $L = 10$ km the one for $L = 30$ km, i.e., over a very short range of scales, is discussed in section 5 through an analysis of the spatial scaling.

5.2. Spatial Scaling

[36] Figure 9a and Figure 9b show $\sigma_{\dot{D}}$ versus the initial separation L, for winter and summer respectively. Errors of $\sigma_{\dot{D}}$ are once again very large and increase as timescale increases and spatial scale decreases.

[37] Similar to the dependence with time, we observe for both seasons a power law spatial scaling, $\sigma_{\dot{D}} \sim L^{-\beta(\tau)}$, over 3 orders of magnitude although this scaling is far from being as well-defined as in the temporal case. In the temporal case, the pairs of buoys considered do not change as we consider different temporal scales, i.e., we look at approximately the same regions for two different τ. In contrast, as L changes, we sample different regions of the Arctic, as the pairs of buoys considered are not the same. So first, this could partly explain the noise seen in the spatial scaling. Second, we expect inhomogeneous forcing at large time or space scales and the influence of the coasts to be possible causes for a bias on the $\sigma_{\dot{D}}$-values. The inhomogeneous forcing arises from the large-scale variability in the mean wind and water stresses over the basin [*Steele et al.*, 1997].

[38] The exponents β were determined using a weighted least squares algorithm. The corresponding uncertainty in β ranges from 15% to 80%. The exponent β increases with decreasing timescale τ, ranging from 0.85 for $\tau = 1$ h to 0.35 for $\tau = 1$ month in winter and from 0.85 for $\tau = 1$ h to 0.42 for $\tau = 1$ month in summer (Figure 10). Once again, winter and summer cannot be distinguished on this basis.

6. Discussion

[39] As a generalization of the examples studied in section 3, the magnitudes of the deformation rates have

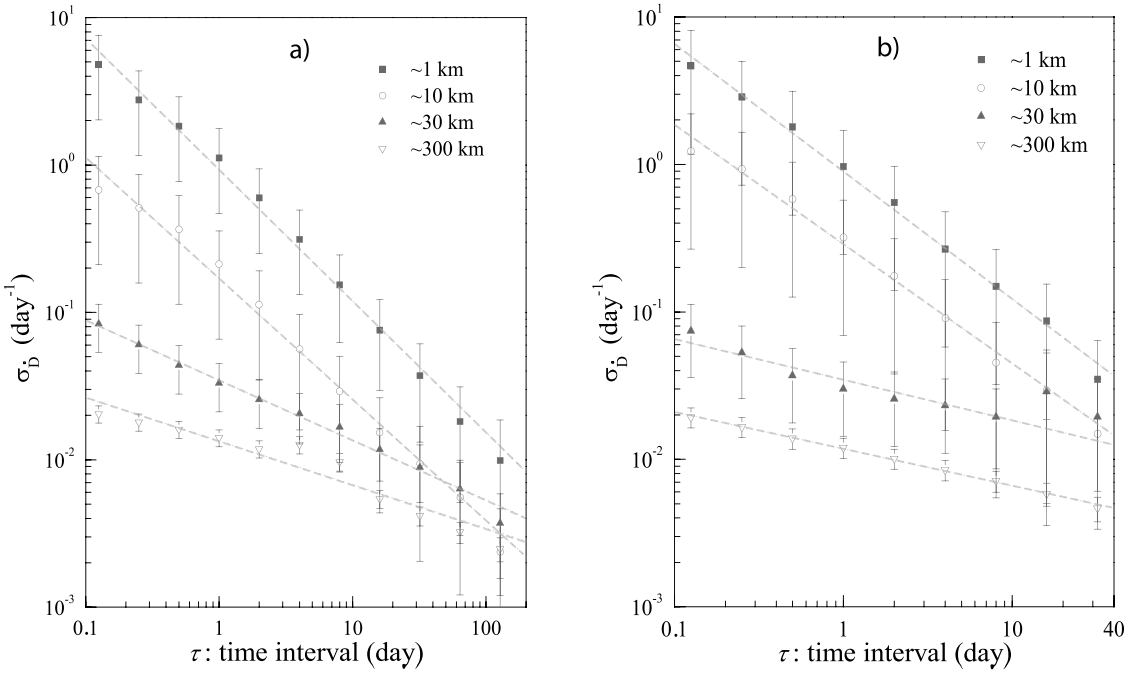

Figure 7. (a). σ_D versus τ for $L \sim 1$, 10, 30, and 300 km, and the winter season. The L-values correspond to the spatial bins: 0.3–2 km, 2–16 km, 16–64 km, and 64–512 km respectively. Error bars are estimated by a bootstrap method (Cf Appendix 1). The gray dashed lines show the best power law fit (in the least squares sense) to the 4 data sets. (b). Same as Figure 7a, for summer.

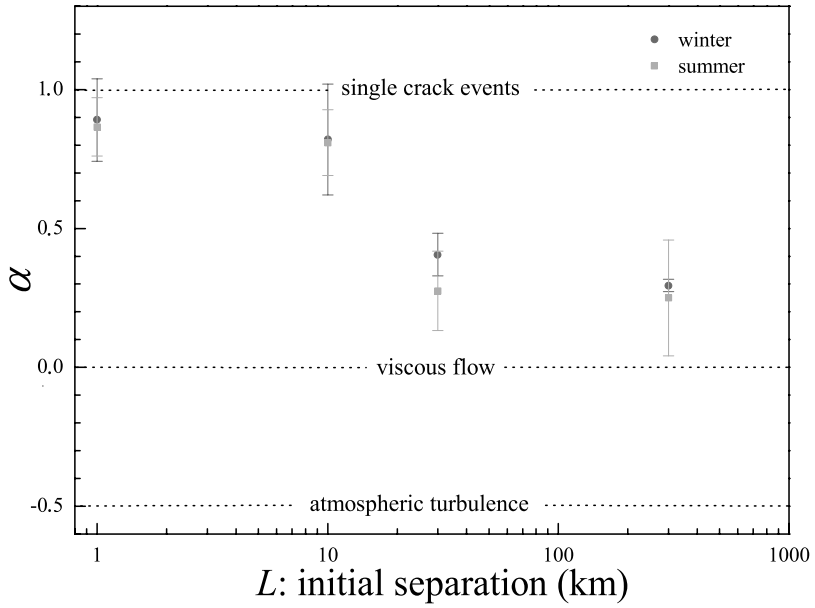

Figure 8. Power law exponent α versus initial separation L for winter (circles) and summer (squares). Dashed lines represent the α -values corresponding to (i) an extremely intermittent deformation process (temporal fractal dimension equals to zero), (ii) a non-intermittent viscous flow, and (iii) atmospheric turbulence.

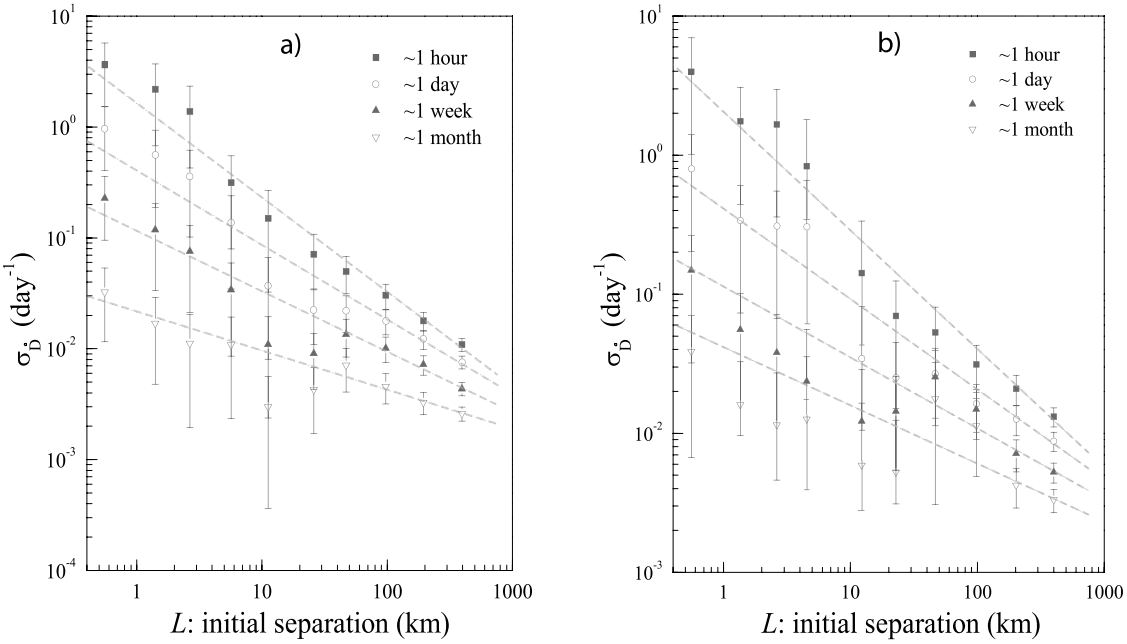

Figure 9. (a). σ_D versus the initial separation L for 3 h $\leq \tau \leq$ 12 h, 1 $\leq \tau \leq$ 4 days, 8 days $\leq \tau \leq$ 16 days, 32 days $\leq \tau \leq$ 128 days, for the winter season. Error bars are estimated by the bootstrap method of Appendix 1. The gray dashed lines show the best power law fit (in the least squares sense) to the 4 data sets. (b). Same as Figure 9a, for summer. The time intervals are redefined as: 3 h $\leq \tau \leq$ 12 h, 1 $\leq \tau \leq$ 4 days, 8 days $\leq \tau \leq$ 16 days, 32 days $\leq \tau \leq$ 64 days.

been shown to depend on L and τ: Deformation rate increases as L and τ decrease. As a point of comparison, the deformation rate in winter for $L > 100$ km and $\tau = 3$ days is about 10^{-2} day^{-1}, which is in close agreement with the estimate of *Marsan et al.* [2004] from RGPS data.

6.1. Time Scaling

[40] Following expression (6), we estimate the exponents γ for the time scaling of the dispersion (i.e., for $\langle \Delta r^2 \rangle \sim \tau^{\gamma}$), from the exponents α observed for the time scaling of the deformation. We find $0.22 < \gamma < 1.44$, from small to large spatial scales L. The deformation of Arctic sea ice appears to follow different regimes, from sub-diffusive (at $L < \sim 10$ km) to super-diffusive (at $L > \sim 10$ km). However, for any particular scale L, we cannot define a characteristic time at which a change in regime occurs. This shows that the time scaling of the dispersion found by *Martin and Thorndike* [1985] and the one found in the SIMI case (see section 3) cannot be considered, in a statistical sense, as representative of general sea ice dynamics. In other words, a variety of time scaling can be found locally, and depends on the spatial scale considered.

[41] The evolution of the time scaling exponent α with increasing spatial scale L (Figure 8) can be interpreted if one considers the deformation of sea ice to be accommodated by a multiscale fracturing process [*Marsan et al.*, 2004]. The exponent α is then a measure of the degree of intermittency of the deformation process: at small L, this process is highly intermittent, and α is close to the unit case $\alpha = 1$ corresponding to deformation accommodated "by a single fracturing event". As L increases, the average effect of an increasing number of fractures causes the deformation to become "smoother" in time, i.e., α decreases. However, α is positive even at the largest spatial scale considered here ($L \sim 300$ km), i.e., sea ice deformation is always intermittent and does not mimic viscous flow. This shows that the hypothesis of viscous flow in sea ice models [*Hibler*, 1977] is not fulfilled, even at very large spatial scales. On the other hand, we are far from the case of atmospheric turbulent dispersion ($\alpha = -0.5$), corresponding to the "t^3 law" [*Richardson*, 1926].

6.2. Spatial Scaling

[42] Just as the time scaling exponent α depends on L, the spatial scaling exponent β depends on the timescale τ (Figures 9a and 9b).

[43] Turbulence theory predicts a characteristic time at which the regime of dispersion changes. *Batchelor* [1960] and *Kraichnan* [1966] showed that, for small τ $\langle \Delta r^2 \rangle \sim L^{2/3}$, and for large τ $\langle \Delta r^2 \rangle \sim L^{4/3}$. Translated in terms of deformation rate, this means that, for small τ σ_D scales as $L^{-2/3}$, and for large τ σ_D scales as $L^{-1/3}$. In our case, a characteristic time cannot be distinguished. The exponent β decreases continuously as τ increases (Figure 10). This leads to the conclusion that time and space scales are strongly coupled and cannot be separated for Arctic sea ice deformation, or, in other words, that the scaling of σ_D does not reduce to $L^{-\beta}\tau^{-\alpha}$.

[44] As α is a measure of the degree of temporal intermittency, β is a measure of the degree of spatial heterogeneity of sea ice deformation. The boundary value $\beta = 2$ would correspond to a highly localized deformation process, e.g., a single fracture in an elastic medium, whereas $\beta = 0$ indicates homogeneous deformation (e.g., elastic or viscous). Here, β is always far from the boundary value $\beta = 2$ and decreases toward large timescale τ, as more and more fracturing events are taken into account. However, it never reaches the homogeneous case ($\beta = 0$), even at large

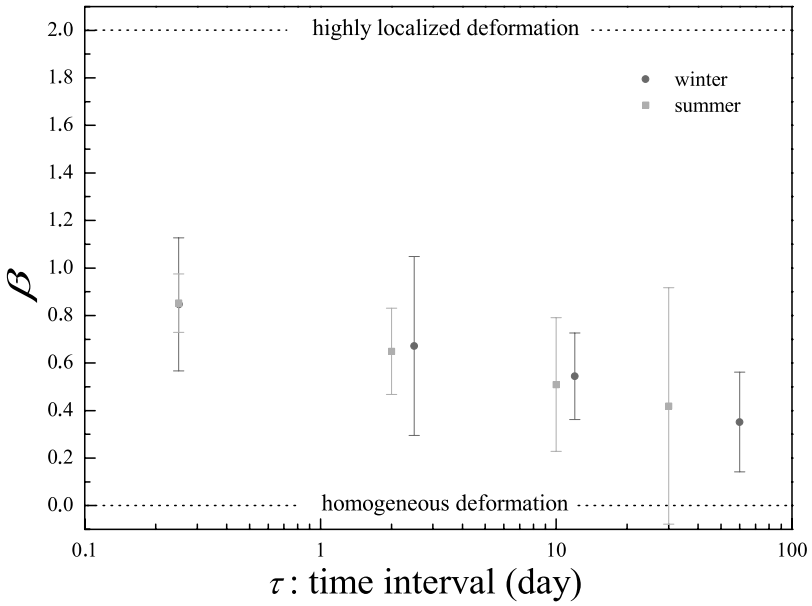

Figure 10. Power law exponents β versus time interval τ for winter and summer. Dashed lines represent two characteristic deformation processes, from a homogeneous one to a highly localized one (spatial fractal dimension equals to zero).

timescales ($\tau \sim 2$ months). Once again, the viscous flow hypothesis is not fulfilled.

[45] Considering the role of oceanic driving, *Okubo* [1971] found from the analysis of buoy dispersion that $\langle \Delta r^2 \rangle \sim L^{1.1}$ for surface oceanic turbulence. This translates into $\beta = 0.45$. This is close to the value obtained at large timescales (Figure 10) for both winter and summer seasons. In other words, sea ice dispersion mimics a free drift, oceanic dispersion only at large timescales (i.e., >1 month). At smaller scales (i.e., <1 month), the elasto-brittle behavior of Arctic sea ice results in a much more heterogeneous and localized deformation. This transition at ~1 month can therefore be viewed as an integral scale at which the sea ice deformation is driven by oceanic forcing.

[46] As shown above, the results of Figure 9a and Figure 9b are compatible, within the large error bars, with a single spatial scaling. However, it is possible to differentiate two different regimes, separated by a transition scale of about 10 km (Figure 11a). The evolution of the corresponding slopes $\beta_{<10\text{km}}$ and $\beta_{>10\text{km}}$ with increasing timescale τ is shown in Figure 11b. A possible interpretation of a change of dispersion regime is related to ocean dynamics. Indeed, this 10 km scale is known to be consistent with a class of dynamical structure in the ocean: an estimation of the internal Rossby radius at northern latitudes leads to the same order of spatial scale. Therefore this possible regime change could indicate the role of oceanic dynamical structures such as eddies. However, owing to the fact that both interpretations (1 or 2 dispersion regimes) are compatible with our results and the associated uncertainties, further studies are needed to definitively answer this question.

6.3. Seasonal Dynamics of Sea Ice

[47] On the basis of the scaling properties summarized in Figure 8 and Figure 10, winter and summer sea ice dynamics cannot be differentiated. Whatever the time or spatial scales considered, the magnitudes of σ_D are very similar in winter and summer, from 10 day^{-1} for small time and spatial scales, to 10^{-3} day^{-1} for large scales. This might appear, at first glance, in contradiction with the expectation that a loose summer ice pack would disperse and deform according to a free drift regime. As shown above, this free drift regime is only recovered at large timescales in both winter and summer. Even if the loose assembly of ice floes characterizing the marginal ice zone bordering the perennial ice pack might behave differently, our results suggest that the perennial sea ice cover of the central Arctic basin (from which most of the buoy observations come; see Figure 1) behaves as a fractured solid plate, just as the winter ice cover does, and not as a free assembly of floes. This may have major implications in terms of global sea ice drift or sea ice mass balance.

6.4. Perspectives for Future Studies

[48] We recall that for the homogeneous deformation of a typical solid (i.e., elastic deformation or viscous flow), the deformation rate does not depend on the time and spatial scales (i.e., $\alpha = 0$ and $\beta = 0$). The present observations argue for sea ice deformation characterized by both intermittency and heterogeneity, and by a strong space-time coupling. The next step would be to quantify this space-time coupling, searching for a general link between the distributions of strain rates at different space and timescales. Then it might be possible to completely characterize the scaling properties of the sea ice deformation and deduce, by downscaling or upscaling, useful information for modelers to use for model validation.

7. Conclusions

[49] In summary, the primary conclusions of our analysis of buoy trajectories are:

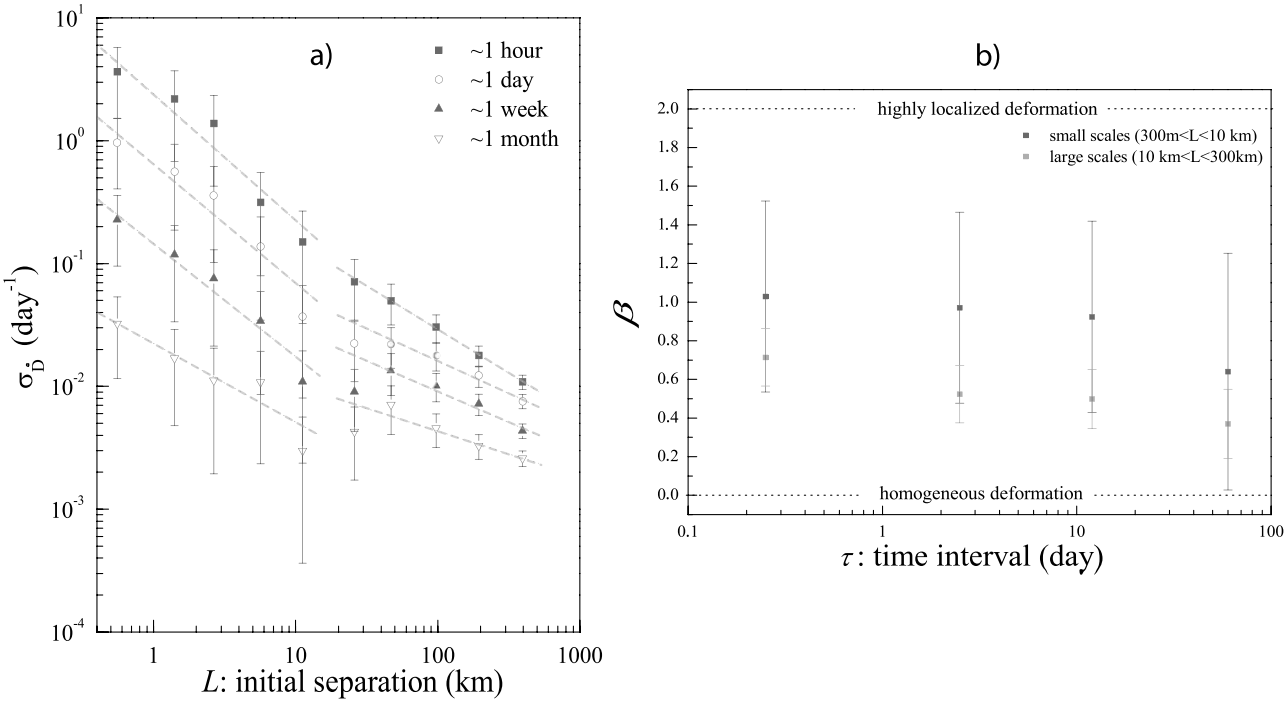

Figure 11. (a). Same as Figure 9a, but with power law fits assuming a regime change at ~10 km. (b). Same as Figure 10, but separating the two space intervals $L < 10$ km and $L > 10$ km (*Cf* Figure 10).

[50] (i) The deformation of sea ice is the result of a highly intermittent and heterogeneous dispersion process.

[51] (ii) The deformation depends on both space and timescales. We showed that it follows a power law model that is scale invariant over several orders of magnitude in time and space.

[52] (iii) The values of the exponents of the power functions depend on both time and space scales. This leads us to conclude that time and space scales are coupled.

[53] (iv) Even for large timescales, i.e., several months, and for the Arctic basin scale, i.e., 1000 km, we showed that Arctic sea ice deformation does not mimic viscous flow, a contradiction to the classical sea ice modeling assumption.

Appendix A: Estimating uncertainties

[54] Time correlations (memory effects) are present in ice velocity records [*Thorndike*, 1986a, 1986b], and can also be

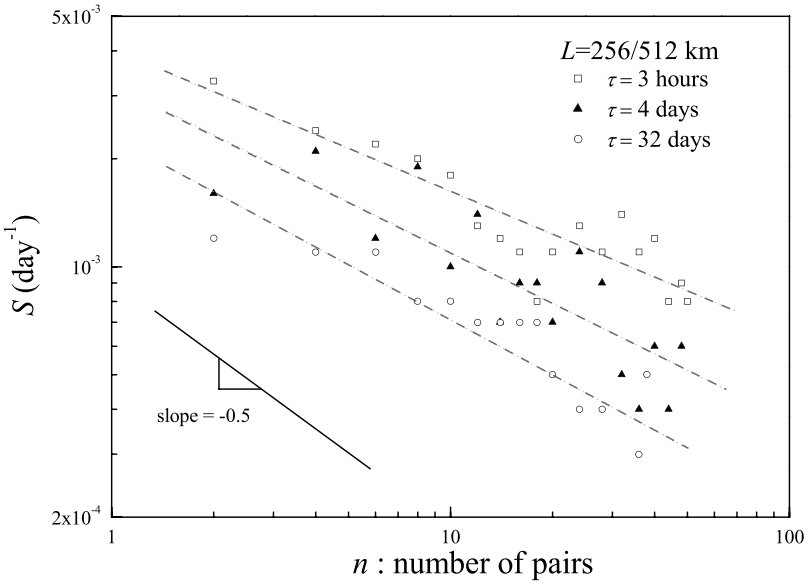

Figure A1. Standard deviation S of $\sigma_{\dot{D}}$ versus the number of pairs n, for the spatial bin 256−512 km and three different time intervals τ. The dashed lines are the best power law fit to the data. The black line with slope −0.5 shows $S(n)$ if the central limit theorem would apply.

found in time series of ice deformation rates as measured by the dispersion of pairs of buoys. An autocorrelation reveals a decorrelation time of about 10 h for an initial separation of $L \sim 300$ km. This decorrelation time becomes smaller for small L. In addition, strong spatial correlations are present in the deformation field [*Marsan et al.*, 2004]. Consequently, the errors on the estimation of $\sigma_{\dot{D}}$ cannot be obtained directly from the central limit theorem and the number N of samples, as it is usually assumed that those N samples are independent of each other. Instead, we estimate these errors from a bootstrap method. It can be shown that the number of pairs of buoys N_p taken into account in each distribution, rather than the number of samples N, should be used as the number of independent variables. N_p ranges from 3 to 686 for winter, and from 1 to 463 for summer. In order to empirically find how the error $\Delta\sigma_{\dot{D}}/\sigma_{\dot{D}}$ depends on N_p, we selected those distributions that contain $N_p \geq 100$ pairs. Then, we randomly picked q times ($q \geq 10$), all the $\sigma_{\dot{D}}$-values coming from n independent pairs of buoys, taking care not to pick the same pair twice, with the condition $q \times n \simeq 0.75 \times N_p$. Then, we obtain, for each couple (L, τ), q distributions of $\sigma_{\dot{D}}$-values for which we calculate their standard deviation S. In other words, the S-values correspond to the dispersion of around its mean, for a given n. Figure A1 shows the results of this method for 3 different distributions corresponding to 3 different couples of scales (L, τ). Finally, we obtain that S decreases with n as:

$$S = \Delta\sigma_{\dot{D}} = f(\sigma_{\dot{D}}, n) = A \times \sigma_{\dot{D}}/n^{\lambda} \qquad \text{(A1)}$$

where $\sigma_{\dot{D}}$ is the value of the standard deviation found for a particular distribution, A is about 0.9, and λ is approximately equal to 0.4. In our analysis, we use this relation to estimate the uncertainty in $\sigma_{\dot{D}}$.

[55] We note that this expression is similar to the error estimate given by the central limit theorem, with the important difference that the number of pairs of buoys N_p is considered instead of the number of samples N. Also, the values of A and λ differ slightly from $A = 1$ and $\lambda = 0.5$ as would be expected if the central limit theorem would apply.

[56] **Acknowledgments.** We thank I. Rigor from the Polar Science Center of Seattle for the compilation and the distribution on the Web of the IABP data set. We also thank J. Richter-Menge and C. Geiger from CRREL who kindly provided the SIMI and SHEBA data sets. The work of R.L. and H.S. was supported by grants from the National Science Foundation. Two anonymous reviewers are greatly thanked for their constructive reviews.

References

Batchelor, G. K. (1951), Diffusion in a field of homogeneous turbulence, 2. The relative motion of particles, *Proc. Cambridge Philos. Soc.*, *48*, 345–362.

Batchelor, G. K. (1960), The theory of Homogeneous Turbulence, 197 pp., Cambridge University Press.

Einstein, A. (1905), Investigations on the theory of the Brownian motion, *Ann. Phys.*, *17*, 549–560.

Heil, P., and W. D. Hibler (2002), Modeling the high-frequency component of Arctic Sea ice drift and deformation, *J. Phys. Ocean.*, *32*, 3039–3056.

Hibler, W. D. (1977), A viscous sea ice law as a stochastic average of plasticity, *J. Geophys. Res.*, *82*(27).

Hibler, W. D. (1979), A dynamic thermodynamics sea ice model, *J. Phys. Ocean.*, *9*, 815–846.

Hunke, E. C., and J. K. Dukowicz (1997), An elastic-viscous-plastic model for sea ice dynamics, *J. Phys. Oceanogr.*, *27*(9), 1849–1867.

Jullien, M. C., J. Paret, and P. Tabeling (1999), Richardson pair dispersion in two-dimensional turbulence, *Phys. Rev Lett.*, *82*(14).

Kraichnan, R. H. (1966), Dispersion of particle pairs in homogeneous turbulence, *Phys. Fluids*, *9*, 1937–1943.

Kwok, R. (1998), The RADARSAT geophysical processor system, in *Analysis of SAR Data of the Polar Oceans*, edited by C. R. Tsatsoulis and R. Kwok, Springer-Verlag, pp. 235–237.

Kwok, R. (2001), Deformation of the Arctic ocean sea ice cover between November 1996 and April 1997: a qualitative survey, in *Scaling Laws in Ice Mechanics*, edited by H. H. Shen, Kluwer Academic, pp. 315–322.

Kwok, R. (2006), Contrasts in sea ice deformation and production in the arctic seasonal and perennial ice zones, *J. Geophys. Res.*, *111*, C11S22, doi:10.1029/2005JC003246.

Marsan, D., J. Weiss, R. Lindsay, and H. Stern (2004), Scale dependence and localization of the deformation of Arctic Sea ice, *Phys. Rev. Let.*, *93*(17).

Martin, S., and A. S. Thorndike (1985), Dispersion of sea ice in the Bering Sea, *J. Geophys. Res.*, *90*(C4), 7223–7226.

Martins, C. S., M. Hamann, and A. F. G. Fiuza (2002), Surface circulation in the eastern North Atlantic from drifters and altimetry, *J. Geophys. Res.*, *107*(C12), 3217, doi:10.1029/2000JC000345.

Maykut, G. A. (1982), Large scale heat exchange and ice production in the central Arctic, *J. Geophys. Res.*, *87*(C10), 7971–7984.

Morel, P., and M. Larchevèque (1974), Relative dispersion of constant-level baloons in the 200-mb general circulation, *J. Atmos. Sc.*, *31*, 2189–2196.

Moritz, R. E., C. M. Bitz, and E. J. Steig (2002), Dynamics of recent climate change in the Arctic, *Science*, *297*, 1497–1502.

Nye, J. F. (1973), Is there any physical basis for assuming linear viscous behaviour for sea ice?, *AIDJEX Bulletin* #21, 18–19, July.

Okubo, A. (1971), Oceanic diffusion diagrams, *Deep Sea Res.*, *18*, 789–802.

Richardson (1926), Atmospheric diffusion shown on a distance-neighbour graph, *Proc. R. Soc. London*, *A110*, 709–737.

Richardson, L. F., and H. Stommel (1949), Note on eddy diffusion in the sea, *J. Meteorol.*, *5*, 238–240.

Steele, M., J. Zhang, D. Rothrock, and H. Stern (1997), The force balance of sea ice in a numerical model of the Arctic Ocean, *J. Geophys. Res.*, *102*, 21,061–21,079.

Taylor, G. I. (1921), Diffusion by Continuous Movements, *Proc. London Math. Soc.* (20), Ser. 2.

Thorndike, A. S. (1986), Sea Ice Kinematics, in *Geophysics of Sea Ice*, edited by N. Untersteiner, Plenum, New York.

Thorndike, A. S. (1986), Diffusion of sea ice, *J. Geophys. Res.*, *91*(C6), 7691–7696.

Thorndike, A. S., and R. Colony (1982), Sea ice motion in response to geostrophic winds, *J. Geophys. Res.*, *87*(C8), 5845–5852.

Weiss, J., and D. Marsan (2004), Scale Properties of Sea Ice Deformation and fracturing, *C. R Physique 5*.

Weiss, J., E. M. Schulson, and H. Stern (2007), Sea ice rheology from in-situ, satellite and laboratory observations: Fracture and friction, *Earth Planet. Sci. Lett.*, *255*, 1–8.

Zhang, H.-M. (2001), Isopycnal Lagrangian statistics from the North Atlantic Current RAFOS float observations, *J. Geophys. Res.*, *106*(C7), (13) 816–836.

Zhang, J., D. Rothrock, and M. Steele (2000), Recent changes in Arctic Sea ice: The interplay between ice dynamics and thermodynamics, *J. Clim.*, *13*(17), 3099–3114.

R. Lindsay and H. Stern, Polar Science Center, Applied Physics Laboratory, University of Washington, Seattle, WA, USA.

D. Marsan, Laboratoire de Géophysique Interne et Tectonophysique, CNRS, Université de Savoie-Le Bourget du Lac, France.

P. Rampal and J. Weiss, Laboratoire de Glaciologie et Géophysique de l'Environnement, CNRS, Université Joseph Fourier-Grenoble, France. (weiss@lgge.obs.ujf-grenoble.fr)